

# Model validation for a noninvasive arterial stenosis detection problem

H.T. Banks, Shuhua Hu and Zackary R. Kenz

Center for Research in Scientific Computation

North Carolina State University, Raleigh, NC 27695-8212

Carola Kruse, Simon Shaw, and John Whiteman

`{carola.kruse, simon.shaw, john.whiteman}@brunel.ac.uk`

BICOM, Brunel University, Uxbridge, UB8 3PH, England.

`www.brunel.ac.uk/bicom`

M.P. Brewin, S.E. Greenwald

`{s.e.greenwald, m.p.brewin}@qmul.ac.uk`

Blizard Institute, Barts and the London School of Medicine and Dentistry,

Queen Mary, University of London, England.

M. J. Birch

`m.j.birch@qmul.ac.uk`

Clinical Physics, Barts Health Trust, England.

June 9, 2013

## Abstract

A current thrust in medical research is the development of a non-invasive method for detection, localization, and characterization of an arterial stenosis (a blockage or partial blockage in an artery). A method has been proposed to detect shear waves in the chest cavity which have been generated by disturbances in the blood flow resulting from a stenosis. In order to develop this methodology further, we use one-dimensional shear wave experimental data from novel acoustic phantoms to validate a corresponding viscoelastic mathematical model. We estimate model parameters which give a good fit (in a sense to be precisely defined) to the experimental data, and use asymptotic error theory to provide confidence intervals for parameter estimates. Finally, since a robust error model is necessary for accurate parameter estimates and confidence analysis, we include a comparison of absolute and relative models for measurement error.

**Mathematics Subject Classification:** 62F12; 62F40; 65M32; 74D05.

**Key words:** viscoelastic model; sensitivity analysis; inverse problem; asymptotic theory.

# 1 Introduction

Coronary artery disease (CAD) is an increasingly prevalent medical condition, often a precursor to and cause of a patient experiencing cardiac arrest. Current methods for detection of arterial stenoses (blocked arteries) include the angiogram and CT scans. Angiograms are viable but quite invasive, while CT scans are expensive, introduce radiation into the patient, and can only detect hard plaques (blockages). A desirable new detection method would be noninvasive and less expensive but still effective. To this end, using acoustic waves generated by stenoses has been proposed. This would place sensors on the surface of the chest to listen for sounds from coronary arteries, with the hope of detecting and then localizing any blockages.

The current understanding (see, e.g., [8, 26, 45]) of the process is that turbulent flow produces normal forces on the vessel walls at and downstream of a stenosis, which then exert pressure on the vessels wall causing a small displacement in the surrounding soft tissue. Previous work (e.g. [2, 32, 46, 43, 44, 52, 56]) has demonstrated the existence of such sounds, and that they are possible to detect on the surface of the chest. We thus see that the system couples two processes: (1) the generation of pressure and shear waves transmitted into the body through the arterial wall as a result of the turbulent blood flow generated by a stenosis, and (2) the propagation of pressure and shear waves through the chest to sensors attached to the chest wall. The first process is not completely understood, though some ideas are present in the literature. Various researchers [24, 25, 26, 36, 39, 41, 45, 48, 49, 55, 59] have directly examined modeling blood flow through arteries. All have attempted to characterize the turbulence in the flow, which some then used to examine the sound field propagated into the chest. In the current work, we will not focus on aspects of turbulent flow, leaving that instead as an input to be later properly characterized when the stenosed artery situation is modeled directly. We will focus on the second process, understanding the propagation of sounds through the chest cavity which result from stenosed coronary arteries.

The modeling and detection of waves transmitted through the body has been approached in different ways. One approach has focused on characterizing properties of the sounds detected on the surface of the chest, characterizing aspects such as primary frequencies that these sounds exhibit. This line of work has been studied by Semmlow, et al., [2, 3, 4, 5, 6, 47, 53, 54, 61], as well as by other groups [24, 25, 26, 34, 46, 56, 57, 58]. Their methods are based on general sound features and detection through statistical methods, rather than modeling the underlying physics of sound transmission through the body. These methods have the benefit of being fast and fairly simple to implement, but do not provide a characterization for the mechanisms of wave transmission.

In another direction, more relevant to the situation this paper will study, researchers have worked to model the physics of sound wave transmission through the body. As is common in many physical wave phenomena, both pressure and shear waves propagate into the body as a result of stenosed coronary arteries. Since shear waves in general have a lower amplitude than pressure waves, intuition might suggest detecting pressure waves should be our focus; past research indicates the opposite is true when seeking to detect stenoses. Various groups [28, 30, 40, 45] have demonstrated that shear waves should be the focus of detection efforts. The frequency ranges for shear waves resulting from coronary stenoses are below 2000 Hz [25, 28, 29, 33, 51, 53]. In the range of these frequencies, the pressure waves propagate very quickly while shear waves propagate much more slowly, which in practice means that pressure waves are difficult to measure. Furthermore, the lower speed of shear waves implies a shorter wavelength for a given frequency, thus providing better spatial resolution when attempting to localize a stenosis. Also, in the context of waves propagating in tissue or tissue-mimicking materials, shear waves are measurable at greater distances from the source of the disturbance (see, e.g., Figures 9b and 10 of [28]). Thus, in this work we also focus on studying a model for shear wave propagation (though results where we also test a pressure wave model are available in a technical report [14]).

The benefits of using a viscoelastic wave propagation model in various contexts have been previously studied [28, 30, 31, 33, 37, 40, 51]. In these references, the authors focused on determining the elastic modulus and viscoelastic parameter based on the shear wave speed and attenuation in either a gel mold or physical tissue, in both a stenosis context and general tissue shear wave propagation. The models were developed using plane waves in such a way that algebraic expressions were available for shear wave speed as a function of frequency, elastic modulus, and the viscoelastic parameter. These demonstrate that modeling the underlying physics is not only possible, but quite beneficial in understanding shear wave propagation. These investigators also showed that a Kelvin-Voigt damping model is most appropriate for the situation; we will incorporate this into our model (and will discuss it more fully below).

In this work, we will take the physical models further, developing a dynamic model of the shear waves propagating through a tissue-mimicking material. Our goal will be to use this viscoelastic model with data from a tissue-mimicking homogeneous gel mold to validate the model and understand the uncertainty in the model parameters. The model here will incorporate the standard elastic modulus and bulk viscoelastic parameter, as well as *internal variables* governed by *relaxation times* which can be used to model how different portions of the medium relax in different

ways from being stressed. We will develop the model in such a way as to allow for multiple internal variables. In future studies these can be used to model the bulk effects of different types of tissue, which would be closer to the *in vivo* detection problem.

The model here will continue from a previous line of work by Banks, et al., [8, 18, 19, 20, 21, 42, 50]. These models allow for a characterization of shear waves resulting from coronary stenoses, which will assist in uncovering the coronary artery sounds from the noisy background in the body. Initial experiments were conducted where a gel mold was built with a tube running through the middle; cases where the tube was unblocked were compared to those with partial blockages, and the results suggested that there were significant differences in sound generation between the blocked and unblocked cases. Unfortunately, this line of work ended before experimental data could be incorporated and used to validate models. The current work returns to a one-dimensional model and experimental setup, developing a model closely related to that in [8] which we validate with lab data from a homogeneous gel phantom and use to examine uncertainty in our parameter estimates. This work will examine confidence in the relaxation times, which will demonstrate that the addition of internal variables into the model is viable.

We now summarize the goals and direction for the current work. Here, we incorporate all of the aforementioned physical modeling concerns and continue the work of our concept paper [13] by focusing on wave propagation through a homogeneous viscoelastic medium. The constitutive relationship will be slightly more general than in our concept paper, and is based on Fung’s viscoelastic formulation that has been validated by actual tissue experimental data (more details below). This relationship will be used in one-dimensional shear wave dynamical models to compute inverse problem results for the one-dimensional case using experimental data from a tissue-mimicking gel mold. This data comes from novel acoustic phantoms built and tested at Queen Mary, University of London (QMUL) and Barts Health Trust (BHT) in England. The data will be taken in such a way that measured displacements upon releasing a load are primarily affected by the properties of the medium. Displacement data for our case encodes the frequency and attenuation properties of the medium, which we then quantify through model parameter estimation. This will firmly set the groundwork for future investigations into validating the model in a more complex medium, as well as investigation into a proper description of an input for the wave propagation model; this input would result from models of the sounds (arterial wall displacements) due to turbulent blood flow resulting from a stenosis.

## 2 Experimental Setup

A novel experiment has been devised at QMUL to gather one-dimensional shear data. Devices have been designed (see left pane of Figure 1), in which an agar gel mold phantom (homogeneous, 97% water, density  $\rho = 1010 \text{ kg/m}^3$ ) is loaded into the rig, a weight is attached applying stress to the phantom, and then the weight is released, causing the material to oscillate. The displacement motion of the material throughout the experiment is measured with a laser device. This motion is due to the material response to the weight release, and thus encodes information about the material characteristics (elastic modulus, damping characteristics, etc.). The choice of loading and a quick release is designed to produce dynamic data; the idea was inspired in part by the impacts the stenosed vessel wall experiences with each heartbeat and also by past success in gathering shear data for filled rubber elastomers using an initially loaded rubber sample which then underwent an impulsive hammer hit (see e.g. [18, 19]). This yields one-dimensional shear data in the radial direction perpendicular to the vertical axis (right pane of Figure 1).

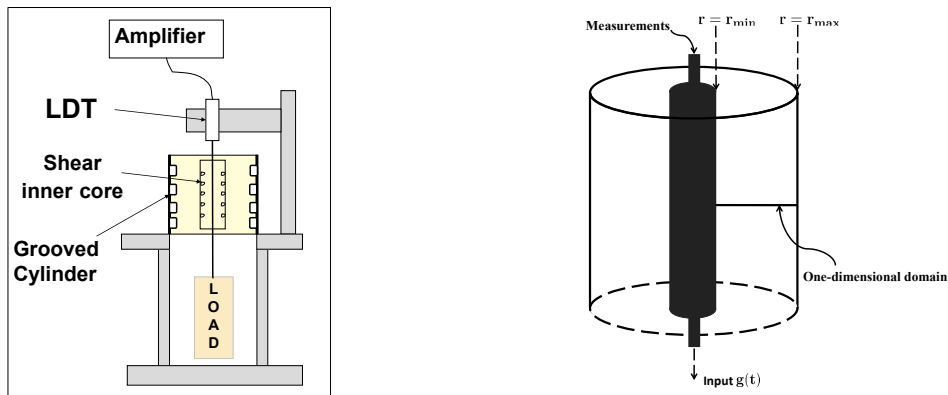


Figure 1: Shear configuration, where LDT denotes the laser displacement transducer. (left) Experimental setup of agar phantom. (right) Schematic with one-dimensional domain denoted.

In this work, we focus on results generated from a load weight of 264 g, as this weight level produces a well-defined response. In the future, we may also incorporate data from smaller weight levels in order to examine the different phantom responses to other weight levels. The gel phantoms were stored in water when not in use, which keeps the gel at the desired 97% water composition.

When the experiment is conducted, data like those depicted in Figure 2 are produced. The material is at rest,

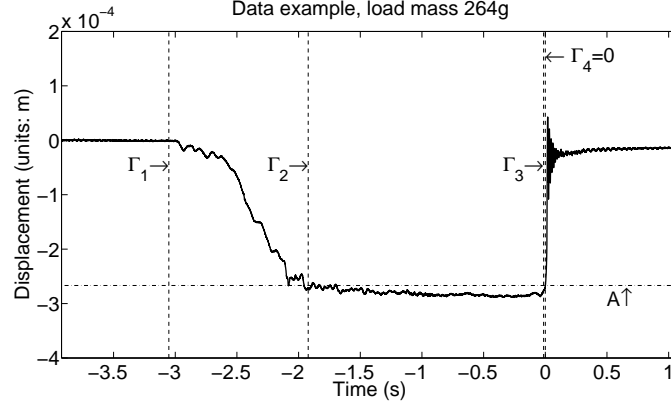


Figure 2: Sample one-dimensional data. Loading of the material (initially at rest) begins at  $t = \Gamma_1$ , and the material is loaded and continues to relax for  $t \in (\Gamma_2, \Gamma_3)$ . At time  $\Gamma_3$  the load is cut which takes roughly 10–15 ms. The gel is then freely oscillating at  $\Gamma_4 = 0$ , and oscillations continue for a period of time dependent on the loading weight. The value  $A$  is the displacement of the material at the beginning of free oscillations. The overall displacement scale of the data is on the order of  $10^{-4}$  m, while the oscillations immediately after the weight release are on the order of  $10^{-5}$  m.

a weight is added and allowed to settle, then the string holding the weight is rapidly cut with a flame to allow the material to freely oscillate. Once oscillations have died out the material relaxes back toward a stable state. The key pieces that will be modeled are the loading profile (loading begins at  $t = \Gamma_1$  and lasts until the weight begins to be released at  $t = \Gamma_3$ ), which we will model as instantaneous loading to position  $A$ , and the oscillations after weight release (free oscillations begin at  $t = \Gamma_4 = 0$ ) which are the main object of investigations here. For more information on the experimental setup, interested readers may refer to [27].

### 3 Model Development and Constitutive Equation

With the setup of the experiment in mind, we can turn to our mathematical model of wave propagation. The model will be developed to take into account all features of the data, including the loading profile and the relaxation present in data. Since our phantom is cylindrical, the model development begins with three-dimensional equations of motion in cylindrical coordinates. These are given in [50, p.20], and also in [42], and are derived from momentum and mass balance principles. Using the fact that the gel is homogeneous and that there are symmetries in the experimental design, these three-dimensional equations can be reduced to simplified one-dimensional model.

Let  $u(r, t)$  represent the displacement of the material at position  $r$  and time  $t$ , with  $r \in (r_{min}, r_{max})$  (for our device,  $r_{min} = 0.0105$  m and  $r_{max} = 0.054$  m) and  $t > \Gamma_1$ , where the time  $\Gamma_1$  is chosen as the beginning of any stress-strain history in the material, and we are assuming the material has been at rest long enough that it is only affected by displacements for  $t > \Gamma_1$ . Then the governing partial differential equation (PDE) becomes

$$\begin{aligned} \rho \frac{\partial^2}{\partial t^2} u(r, t) - \frac{\partial}{\partial r} \sigma(r, t) - \frac{\sigma(r, t)}{r} &= 0 \\ \sigma(r_{min}, t) &= g(t), \quad u(r_{max}, t) = 0 \\ u(r, \Gamma_1) &= 0, \quad u_t(r, \Gamma_1) = 0, \end{aligned} \tag{1}$$

where  $\rho$  is the density of the material,  $\sigma$  denotes the stress,  $g(t)$  is a function that describes the loading process (to be discussed later). In order to complete these models, we must provide a form for  $\sigma$ . This is the constitutive relationship, also called the stress-strain law since it relates strain ( $\frac{\partial u}{\partial r}$ ) and/or the strain rate to stress  $\sigma$ . The next sections discuss this aspect of the model.

### 3.1 Constitutive equation

We incorporate the previous modeling ideas together into a new constitutive equation for the shear wave PDEs (1). We develop the constitutive equation which will be used in this work assuming that we will be solving the model starting at  $t = \Gamma_1$  and thus incorporating both the loading process and oscillations into our dynamic equations, for the time being. In Section 3.1.5, we will make an approximation to the loading process which will allow us to focus on the dynamic oscillations of the material after the weight is released, which is our true interest.

#### 3.1.1 Fung's quasi-linear viscoelastic formulation

Some of the initial investigation into the viscoelastic nature of tissue was completed by Fung [35]. His work is of particular interest because it was validated in actual tissue. Fung developed a “quasi-linear” model

$$\sigma(t) = \int_{\Gamma_1}^t \mathcal{G}(t-s) \frac{d\sigma^e(\lambda(s))}{ds} ds \quad (2)$$

with a kernel of the form

$$\mathcal{G}(t) = \frac{1 + c \int_{\tau_1}^{\tau_2} \frac{1}{\tau} \exp(-t/\tau) d\tau}{1 + c \ln(\tau_2/\tau_1)}. \quad (3)$$

Within (2),  $\lambda$  represents the stretch of a material ( $\lambda = 1 + u_r$ ) and  $\sigma^e$  describes the elastic response to the elongation  $\lambda$ , given by (see [35, Sec. 7.6])

$$\sigma^e(\lambda) = -\beta + \beta e^{\alpha u_r}$$

where  $\alpha$  and  $\beta$  are constants to be estimated. The parameters  $\tau_1$  and  $\tau_2$  are lower and upper bounds, respectively, on *relaxation times*, which describe the ways in which the material responds to imposed stresses and strains. This model incorporates a continuum  $\tau \in [\tau_1, \tau_2]$  of relaxation times, which Fung found to be necessary in order for his model to match the response of tissue, as well as a constant term in the kernel. This Fung kernel will serve as a baseline for reference when developing the model for this paper.

#### 3.1.2 Linearized constitutive equation

One could keep nonlinearities in the constitutive equation (2). However, we found (as we shall see later) that a linear constitutive relationship gives a reasonable approximation to the data provided by QMUL and BHT. To that end, we will use the first two terms of the Taylor expansion of  $e^{\alpha u_r}$  to approximate

$$\sigma^e \approx -\beta + \beta(1 + \alpha u_r) = \beta \alpha u_r = \zeta u_r \quad (4)$$

where we have combined  $\zeta = \beta \alpha$  into a single parameter to be estimated;  $\zeta$  will be incorporated into other parameters later in model development. We can then linearize (2) by using (4), add a Kelvin-Voigt damping term (a common linear viscoelastic damping model [12]), and obtain

$$\sigma(t) = G_1 u_{rt}(t) + \zeta \int_{\Gamma_1}^t \mathcal{G}(t-s) \frac{du_r(s)}{ds} ds \quad (5)$$

where  $\mathcal{G}(t)$  is a kernel to be specified. To an extent, the Kelvin-Voigt term describes the overall nature of the damping present in the material, while the kernel  $\mathcal{G}(t)$  will incorporate different material responses at both the macroscopic and microscopic levels.

#### 3.1.3 Existence and uniqueness for shear wave model

Before moving on to the specific form of the constitutive equation kernel, we first establish existence and uniqueness for the shear wave equations (1) with the constitutive equation (5). To that end, we set up a similar framework as in the concept paper [13] and connect those results to the current work. We will require that the following assumptions hold:

- (A1) The boundary condition function satisfies  $g \in \mathcal{L}^2(\Gamma_1, T)$ ;
- (A2) The kernel  $\mathcal{G}$  is differentiable with respect to  $t$  and with constants  $c_1$  and  $c_2$  such that  $|\mathcal{G}(t)| \leq c_1$  and  $|\dot{\mathcal{G}}(t)| \leq c_2$  for all  $t \in [\Gamma_1, T]$ .

Let  $\mathbb{H} = \mathcal{L}^2(r_{min}, r_{max})$ ,  $\mathbb{V} = \{\phi | \phi \in \mathcal{H}^1(r_{min}, r_{max}), \phi(r_{max}) = 0\}$ , and  $\mathbb{V}^*$  denote the topological dual space of  $\mathbb{V}$ . We identify  $\mathbb{H}$  with its topological dual  $\mathbb{H}^*$  and thus again obtain  $\mathbb{V} \hookrightarrow \mathbb{H} = \mathbb{H}^* \hookrightarrow \mathbb{V}^*$  as a Gelfand triple. Let  $\mathcal{C}_w(\Gamma_1, T; \mathbb{V})$  denote the set of weakly continuous functions in  $\mathbb{V}$  on  $[\Gamma_1, T]$ , and  $\mathcal{L}_T = \{v : [\Gamma_1, T] \rightarrow \mathbb{H} \mid v \in \mathcal{C}_w(\Gamma_1, T; \mathbb{V}) \cap \mathcal{L}^2(\Gamma_1, T; \mathbb{V}) \text{ and } v_t \in \mathcal{C}_w(\Gamma_1, T; \mathbb{H}) \cap \mathcal{L}^2(\Gamma_1, T; \mathbb{V})\}$ . The notion of weakly continuous (i.e.,  $u^m \rightarrow u$  in  $\mathcal{C}_w(\Gamma_1, T; \mathbb{V})$ ) means that  $u^m \rightarrow u$  weakly in  $\mathbb{V}$  and uniformly in  $t \in [\Gamma_1, T]$ . Then a weak solution  $u \in \mathcal{L}_T$  for the shear equation must satisfy

$$\begin{aligned} 0 = & \rho \langle u_t(t), \eta_t(t) \rangle - \rho \int_{\Gamma_1}^t \langle u_s(s), \eta_s(s) \rangle ds + \int_{\Gamma_1}^t g(s) \eta(r_{min}, s) ds + G_1 \int_{\Gamma_1}^t \langle u_{sr}(s), \eta_r(s) \rangle ds \\ & + \zeta \int_{\Gamma_1}^t \left\langle \int_{\Gamma_1}^s \mathcal{G}(s - \xi) \frac{d}{d\xi} u_r(\xi) d\xi, \eta_r(s) \right\rangle ds - G_1 \int_{\Gamma_1}^t \int_{r_{min}}^{r_{max}} \frac{u_{rt}(r, s)}{r} \eta(r, s) dr ds \\ & - \zeta \int_{\Gamma_1}^t \int_{r_{min}}^{r_{max}} \left( \int_{\Gamma_1}^s \frac{1}{r} \mathcal{G}(s - \xi) \frac{d}{d\xi} u_r(r, s) d\xi \right) \eta(r, s) dr ds \end{aligned} \quad (6)$$

for any  $t \in [\Gamma_1, T]$  and  $\eta \in \mathcal{L}_T$  and where  $\langle \cdot, \cdot \rangle$  is the usual inner product. Since  $r_{min} > 0$ , there are no singularities in the final term in (6), and the kernel integral in the numerator of that term will converge in the same manner as the preceding kernel integral. Thus, the arguments from [13] apply in our case here, and we have the following theorem:

**Theorem 3.1.** *Assuming (A1) and (A2), the shear equation (1) with constitutive relationship (5) has a unique weak solution on any finite interval  $[\Gamma_1, T]$ .*

### 3.1.4 Form for constitutive equation kernel $\mathcal{G}(t)$

We will now state the particular kernel used for this current work, and then manipulate it into a form that gives more physical insight and which will later allow for a conceptual framework using *internal variables*. We develop this kernel from a different perspective than that given in [13], but the resulting form will be quite similar. Using the notation and parameter conventions of [12], we define the kernel in this work to be

$$\mathcal{G}(t; P) = \kappa_r + K(t; P) \quad (7)$$

where  $\kappa_r$  is a positive constant representing an instantaneous relaxation modulus (justified by the fact that our gel phantom acts partly as a solid) and  $K(t; P) = \int_{\mathcal{T}} \exp(-t/\tau) dP(\tau)$  represents a continuum of distributed relaxation times with  $\mathcal{T} = [\tau_1, \tau_2] \subset (0, \infty)$  and where  $P(\tau)$  is a probability measure on  $\mathcal{T}$ . Note that this form for  $\mathcal{G}$  satisfies  $|\mathcal{G}(t)| \leq c_1$  with  $\mathcal{G}$  clearly differentiable and  $|\dot{\mathcal{G}}(t)| \leq c_2$  for some constants  $c_1, c_2$  so that assumption (A2) is satisfied. It is also worth noting here that our proposed kernel form (7) is similar to that in Fung's model (3), as we see that  $\kappa_r$  serves as an analog to the constant portion of Fung's kernel (i.e.,  $\frac{1}{1 + c \ln(\tau_1/\tau_1)}$ ) and the  $K(t; P)$  portion is similar to the continuous relaxation spectrum in Fung's model (i.e.,  $\frac{c \int_{\tau_1}^{\tau_2} \frac{1}{\tau} \exp(-t/\tau) d\tau}{1 + c \ln(\tau_2/\tau_1)}$ ).

We substitute (7) into (5) and manipulate the form of the stress with integration by parts, noting that  $u_r(\Gamma_1) = 0$  since the material is initially at rest and using the fact that  $K(0; P) = 1$ :

$$\begin{aligned} \sigma(t; P) &= G_1 u_{rt}(t) + \zeta \int_{\Gamma_1}^t \mathcal{G}(t - s) \frac{du_r(s)}{ds} ds \\ &= G_1 u_{rt}(t) + \zeta \int_{\Gamma_1}^t (\kappa_r + K(t - s; P)) \frac{du_r(s)}{ds} ds \\ &= (G + \zeta) u_r(t) + G_1 u_{rt}(t) - \zeta \int_{\Gamma_1}^t \frac{\partial K(t - s; P)}{\partial s} u_r(s) ds, \end{aligned} \quad (8)$$

where  $G = \kappa_r \zeta$  and with slightly more detail in [14]. This equation (8) is the general form of the constitutive equation used here. The value  $G_0 = G + \zeta$  can be considered to be a dynamic analog to the static shear modulus; this also makes clear the fact that Hooke's Law is incorporated into our model. We have already discussed that  $G_1$  is the bulk damping parameter for the Kelvin-Voigt damping term. The final integral represents a history term which describes the relaxation of the material in response to an applied stress/strain.

We will ultimately turn to a discretized distribution model (using a discrete measure  $P(\tau)$ ), and connect it to the continuum model through a probability measure approximation as in [9]. This will allow us to develop a computationally feasible inverse problem, and also give insight into the underlying material mechanics. But first we briefly discuss a method for approximating the loading process.



### 3.1.5 Approximating the loading process

Recalling Figure 2, the loading profile is relatively long compared with the oscillatory period; since our concern is with modeling the oscillations, solving the model from  $\Gamma_1$  is much longer than necessary. Also, early experimentation with the model indicated that the parameters governing the loading and resting process may differ from those governing the very dynamic post-release oscillatory process.

We address these concerns by modeling the loading as instantaneous from at rest to a displacement of  $A$  at position  $r = r_{min}$ . Since the material is linear, this would then mean the phantom has the profile

$$u(r, t) = \frac{A(r_{max} - r)}{r_{max} - r_{min}}, \quad (9)$$

up until the time of the weight release. Since this is an approximation, we will neglect the times  $t \in (\Gamma_3, \Gamma_4)$ , the weight release time period, since that time frame is small relative to the loading and settling time from  $\Gamma_1$  to  $\Gamma_3$ . We also incorporate a time parameter  $\Upsilon$  which will represent our approximation of the time when loading begins. In the formulation here we will use the same relaxation times during the loading process as during the oscillation period, which means that  $\Upsilon$  has no meaning other than as a tuning parameter that we must estimate. Thus, we assume the given loading profiles for  $t \in (\Upsilon, 0)$  since  $\Gamma_4 = 0$  in our convention. This also means that  $\Upsilon < 0$ .

We incorporate this loading approximation into our model by manually integrating the constitutive relationship (8). For the purposes here, we will call  $\hat{\sigma}$  the full constitutive relationship for  $t > \Upsilon$  that is described by (8) (where we now use  $\Upsilon$  in the place of  $\Gamma_1$ ), and  $\sigma$  the constitutive relationship for  $t > 0$ . We do this for notational simplicity in the final model, at the expense of some minor notational confusion at the current stage. Note that (9) implies that

$$u_r(r, t) = -\frac{A}{r_{max} - r_{min}}, \quad t \in (\Upsilon, 0).$$

Hence, by (8) and the above equation we find

$$\begin{aligned} \hat{\sigma}(t; P) &= (G + \zeta) u_r(t) + G_1 u_{rt}(t) - \zeta \int_{\Upsilon}^t \frac{\partial K(t-s; P)}{\partial s} u_r(s) ds \\ &= (G + \zeta) u_r(t) + G_1 u_{rt}(t) - \zeta \int_{\Upsilon}^0 \frac{\partial K(t-s; P)}{\partial s} u_r(s) ds - \zeta \int_0^t \frac{\partial K(t-s; P)}{\partial s} u_r(s) ds \\ &= (G + \zeta) u_r(t) + G_1 u_{rt}(t) + \zeta \frac{A}{r_{max} - r_{min}} (K(t; P) - K(t - \Upsilon; P)) - \zeta \int_0^t \frac{\partial K(t-s; P)}{\partial s} u_r(s) ds \\ &= \sigma(t; P) - \mathcal{F}(t; \Upsilon, A, P), \end{aligned}$$

where  $\sigma$  and  $\mathcal{F}$  are respectively given by

$$\sigma(t; P) = (G + \zeta) u_r(t) + G_1 u_{rt}(t) - \zeta \int_0^t \frac{\partial K(t-s; P)}{\partial s} u_r(s) ds, \quad (10)$$

and

$$\mathcal{F}(t; \Upsilon, A, P) = -\zeta \frac{A}{r_{max} - r_{min}} (K(t; P) - K(t - \Upsilon; P)).$$

By (10), we then have the following:

- $\hat{\sigma}_r = \sigma_r$
- The original stress boundary condition is  $\hat{\sigma}(r_{min}, t) = 0$  for  $t > 0$ . Using the preceding development, this corresponds with

$$0 = \sigma(r_{min}, t; P) - \mathcal{F}(t; \Upsilon, A, P)$$

which allows us to write the boundary condition for a model solved for  $t > 0$  as

$$\sigma(r_{min}, t; P) = \mathcal{F}(t; \Upsilon, A, P).$$

We note that the term  $\frac{\hat{\sigma}}{r} = \frac{\sigma}{r} - \frac{\mathcal{F}(t; \Upsilon, A, P)}{r}$  results in a time-dependent forcing term in the shear PDE.

We make two comments before discussing the internal variable forms. First, if we assume, for example, a single relaxation time and that its value is small, say on the order of  $10^{-1}$ , then the term  $K(t - \Upsilon; P) = \exp(-(t - \Upsilon)/\tau_1) \approx$

$\exp(-10(t - \Upsilon))$  attains its maximum value  $\exp(10\Upsilon)$  when  $t = 0$ . Note that for, say,  $\Upsilon < -1$ , this term is negligible. Relaxation times on this order are what we can later obtain in the inverse problem, which would imply that in our case the material is at rest after being loaded sufficiently long that it “forgets” its loading history by the time the weight is released. This is good from an experimental standpoint, since the loading process will never be quite uniform. It is also good to know from a computational perspective; we can limit  $\Upsilon$  to being greater than some value, such as  $-20 < \Upsilon < 0$ , which will keep the optimization algorithm from marching off unnecessarily (which occurred in some of our early inverse problem tests). Second, since we have integrated out the loading history, we now start the model at the time of weight release,  $t = 0$ . This means that the material is considered at rest just prior to the release; thus, in the history integrals we will discuss in the next section, all the history now starts at  $t = 0$  since the history before that point will be incorporated into the initial loading profile and an initial stress condition.

### 3.1.6 Internal variable formulation

In the previously noted work on this stenosis problem, the double integrals that resulted from using the continuum of relaxation times in the stress equation were computationally intractable so another approach was required. The idea was to use a discrete number of internal variables. As will be noted, these gave rise to a differential form which was an improvement computationally since it led to purely differential equations in the model rather than inclusion of an integro-differential equation. With the advances in desktop computation abilities since that time, the integral form is now reasonable to use in a dynamic model. However, internal variables are still attractive in that they provide a formulation that indicates some of the internal material dynamics. Physically, if we assume that the molecules within the biological tissue are on a microscopic scale then the portion of the material which is represented by each internal variable or internal strain  $\epsilon_j$  is being driven by the overall strain and has a response that varies depending on the value of the corresponding relaxation time  $\tau_j$ .

Previous work [8, 42, 50] assumed a discrete internal variable form as an approximation to the Fung kernel, using the nonlinear constitutive equation (2). This discrete form assumed the kernel  $\mathcal{G}(t)$  was in an exponential form, with the effects brought together as a discrete sum in the constitutive equation. The results in [8, 42, 50] demonstrate that the internal variable approach is valid and does appear to work as well as the continuum of times in the Fung kernel. A connection between the Fung’s kernel and the discrete kernel is provided by the work in [20]. The authors there form the kernel  $\mathcal{G}(t) = \int_{\mathcal{T}} q(t; \tau) dP(\tau)$  where  $\mathcal{T} = [\tau_1, \tau_2] \subset (0, \infty)$  is the set of admissible relaxation times,  $P(\tau)$  is a probability measure on  $\mathcal{T}$ , and  $q(t; \tau)$  is a continuous function of relaxation times. If we take  $q(t; \tau) = \exp(-t/\tau)$ , this corresponds with the kernels previously discussed. The authors showed existence and uniqueness results for this kernel in the nonlinear constitutive equation (2). Then, a result from [9] allows one to approximate any measure  $P(\tau)$  with a discrete measure. This discrete measure approximation leads us back to the case with a sum of exponentials, but from the probabilistic framework we know conclusively that we are approximating the continuous spectrum of Fung’s kernel and that this approximation has been viable when implemented.

With this background on previous work using internal variables in hand, we move forward by modifying our current model. We manipulate the form of Equation (10) as follows:

$$\begin{aligned} \sigma(t; P) &= (G + \zeta) u_r(t) + G_1 u_{rt}(t) - \zeta \int_0^t \frac{\partial K(t-s; P)}{\partial s} u_r(s) ds \\ &= (G + \zeta) u_r(t) + G_1 u_{rt}(t) - \zeta \int_0^t \frac{\partial}{\partial s} \left( \int_{\mathcal{T}} \exp(-(t-s)/\tau) dP(\tau) \right) u_r(s) ds \\ &= (G + \zeta) u_r(t) + G_1 u_{rt}(t) - \zeta \int_{\mathcal{T}} \epsilon_1(t; \tau) dP(\tau), \end{aligned} \tag{11}$$

where we let  $\epsilon_1(t; \tau) = \int_0^t \frac{\partial}{\partial s} (\exp(-(t-s)/\tau)) u_r(s) ds$ . Rather than the integral form for  $\epsilon_1$ , we can use the differential form

$$\tau \frac{d}{dt} \epsilon_1(t; \tau) + \epsilon_1(t; \tau) = u_r(t), \quad \epsilon_1(0; \tau) = 0 \tag{12}$$

which is then solved simultaneously with the rest of the model dynamics. This is then an *internal variable* or *internal strain*, driven by the overall strain  $u_r(t)$ , which is the continuous form of the internal variable formulation.

We now may finally make the discrete assumption

$$P(\tau) = \sum_{j=1}^{N_p} p_j \Delta \tau_j$$



where  $\Delta_{\tau_j}$  is the Heaviside function with step at  $\tau_j$ , and  $p_j$  are the proportions of the material subject to relaxation time  $\tau_j$  so that  $\sum_{j=1}^{N_p} p_j = 1$ . By substituting this discrete  $P$  into the form for  $\sigma$  as developed in (11), we obtain the discrete, internal variable form of the constitutive relationship

$$\sigma(t) = \left( G + \sum_{j=1}^{N_p} \zeta_j \right) u_r(t) + G_1 u_{rt}(t) - \sum_{j=1}^{N_p} \zeta_j \epsilon^j(t), \quad (13a)$$

with internal variables obeying (for  $j = 1, 2, \dots, N_p$ )

$$\tau_j \frac{d}{dt} \epsilon^j(t) + \epsilon^j(t) = u_r(t), \quad \epsilon^j(0) = 0, \quad (13b)$$

and where we have defined  $\zeta_j = \zeta p_j$  so that  $\zeta = \sum_{j=1}^{N_p} \zeta_j$ , and  $\epsilon^j = \epsilon_1(\cdot; \tau_j)$ .

### 3.2 Final shear wave model

We now put together the shear wave equation (1), using the constitutive equation (13) but with the loading history approximation incorporated as discussed in Section 3.1.5. Recall also that the discrete assumption for  $P$  and the form of  $K$  gives us

$$\zeta K(t; P) = \zeta \sum_{j=1}^{N_p} p_j \exp(-t/\tau_j) = \sum_{j=1}^{N_p} \zeta_j \exp(-t/\tau_j).$$

These equations are just manipulated versions of the general equations of Theorem 3.1, so we still know a unique weak solution exists on any finite time interval.

The shear wave equation, solved for  $t > 0$  which is the release time, are then

$$\begin{aligned} \rho \frac{\partial^2}{\partial t^2} u(r, t) - \frac{\partial}{\partial r} \sigma(r, t) - \frac{\sigma(r, t)}{r} &= \frac{1}{r} \frac{A}{r_{max} - r_{min}} \left[ \sum_{j=1}^{N_p} \zeta_j \exp(-t/\tau_j) - \sum_{j=1}^{N_p} \zeta_j \exp(-(t - \Upsilon)/\tau_j) \right] \\ \sigma(r_{min}, t) &= \frac{-A}{r_{max} - r_{min}} \left[ \sum_{j=1}^{N_p} \zeta_j \exp(-t/\tau_j) - \sum_{j=1}^{N_p} \zeta_j \exp(-(t - \Upsilon)/\tau_j) \right], \quad u(r_{max}, t) = 0 \\ u(r, 0) &= \frac{A(r_{max} - r)}{r_{max} - r_{min}}, \quad u_t(r, 0) = 0, \end{aligned} \quad (14a)$$

where

$$\sigma(t) = \left( G + \sum_{j=1}^{N_p} \zeta_j \right) u_r(t) + G_1 u_{rt}(t) - \sum_{j=1}^{N_p} \zeta_j \epsilon^j(t) \quad (14b)$$

with the internal variables subject to (for  $j = 1, 2, \dots, N_p$ )

$$\tau_j \frac{d}{dt} \epsilon^j(t) + \epsilon^j(t) = u_r, \quad \epsilon^j(0) = 0. \quad (14c)$$

We note that  $G_0 = G + \sum_{j=1}^{N_p} \zeta_j$  is the dynamic analog of the shear modulus.

### 3.3 Numerical method

The shear wave model (14) is numerically solved by using the high order space-time finite element method. Specifically, in time, we use a discontinuous Galerkin method composed of normalized Legendre polynomials (of order 4). In space, we use a continuous spectral finite element method composed of Lagrange basis functions on Gauss-Lobatto nodes (also of order 4). Under this scheme, the system matrices are diagonalizable (this could be lost if we did not use normalized Legendre polynomials in time), and hence the time-coupled computations within a time step can be decoupled. This makes the reasonably high order finite element time discretizations feasible. An argument for adopting such higher order schemes instead of the lower order ones is that higher order spatial discretizations

have been found highly desirable for wave equations in terms of the control of dispersion errors (e.g., see [1, 23]). Moreover, higher order schemes are capable of providing higher fidelity solutions than lower order schemes for the same amount of computational work. This is especially important to make the inverse problem practical (as each inverse problem may require solving the forward problem (i.e., shear wave model) hundreds of times). Further details on this numerical method are in a forthcoming BICOM report [38], wherein an extensive set of numerical results are given to demonstrate the favorable effect on the numerical error and computational work of the higher order temporal and spatio-temporal approximations.

## 4 Inverse Problem

With models in hand, we now turn to matching the model output to data. We will use two common methods in order to estimate model parameters. One is ordinary least squares (OLS) and the other is generalized least squares (GLS). These will be defined later in Section 4.1.

As discussed in Section 2, an experiment has been designed to gather one-dimensional shear data. Measurements in our experiment are taken at  $r = r_{min}$ , and will be denoted by  $u_j$  at measurement time point  $t_j$ . Corresponding shear model solutions at the same spatial location will be denoted  $u(t_j; 10^\theta)$ , where the measurement location has been suppressed for notation convenience and where  $\theta$  represents a vector of the base-10 logarithm of each parameter (the same idea used previously [13] to reduce parameter scaling issues). The data set has been trimmed to the dynamic oscillations after the release, and thus the time frame is 200 ms. The data were sampled at a rate of 2048 Hz; however, this high rate proved to make the inverse problem difficult and computationally intractable because that many data points resulted in the inverse problem being over determined. Instead, we will use every other data point from the larger data set for a sampling rate of 1024 Hz which will we later refer to as the “every data point” set. We take  $n$  to be the total number of data points for a particular data set, and thus can describe the measurement time points for the full “every data point” set as  $t_j = j/1024$  where  $j = 0, 1, \dots, n-1$ . There will also be a reduced data set where we take every other data point starting with  $t_0 = 0$ , which corresponds with a data sampling rate of 512Hz.

Since some of the data points were near zero in absolute value, we found that those points resulted in scaling problems when using the GLS model to estimate model parameters (since the corresponding cost functional divides by the model value as we will see later when this method is defined). To account for this, we removed from consideration any data points  $u_j$  where  $|u_j| < 5 \times 10^{-6}$ . This value was chosen by examining the data, noting that the data is on the order of  $10^{-5}$  and that the “jitter” one can see in Figure 2 has a magnitude of roughly  $5 \times 10^{-6}$  during the times before loading up to  $\Gamma_1$ , then during the settling period from  $\Gamma_2$  to  $\Gamma_3$ , and again in the settling period after the oscillations have died out. Thus, our threshold level is below the level of noise in the data. This level also eliminated only a few data points, while providing significantly improved GLS robustness. The number of data points  $n$  is then reduced according to how many thresholded data points were removed.

Before going into the setup and results for the inverse problem, we note that the forward (i.e., direct) problem where we solve for displacement (using the method discussed in Section 3.3) is as follows:

- **Forward problem:** Given  $G$ ,  $G_1$ ,  $\tau_j$  and  $\zeta_j$  for  $j = 1, 2, \dots, N_p$ ,  $\Upsilon$ ,  $A$ ,  $r_{min}$ ,  $r_{max}$ , and  $\rho$ , solve model (14) for displacement  $u(r, t)$  at each position  $x \in [r_{max}, r_{min}]$  for  $t \in [0, T]$ .

The inverse problem we will develop here is as follows:

- **Inverse problem:** Given shear displacement data at  $r = r_{min}$  and a corresponding forward problem solver for displacement, along with specified values for  $\rho$ ,  $r_{min}$ , and  $r_{max}$ , find values for the constants  $G$ ,  $G_1$ ,  $\tau_j$  and  $\zeta_j$  (for  $j = 1, 2, \dots, N_p$ ),  $A$ , and  $\Upsilon$  which provide the best fit to the data (in a manner which will be defined shortly).

We assume that the parameters lie in some admissible set  $Q \subset \mathbb{R}^\kappa$ , where  $Q$  is assumed to be compact and  $\kappa$  is the number of parameters requiring estimation. Throughout the remainder of this work, we will denote the log-scaled parameter vector (for  $N_p = 1$  and  $\kappa = 6$ ) as

$$\theta = (\log_{10}(G), \log_{10}(G_1), \log_{10}(\zeta_1), \log_{10}(\tau_1), \log_{10}(-A), \log_{10}(-\Upsilon)). \quad (15)$$

Thus, as long as we define our cost function to be a continuous function of the parameters, we know the inverse problem has a solution (minimizing a continuous function on a compact parameter space). One could broaden this parameter estimation framework to the distributional case if desired, taking an admissible parameter space as a compact subset of Euclidean space (including all parameters excluding relaxation times) along with the space of probability measures, and use the Prohorov metric framework (see, e.g., [7, 15, Sec. 4]) and the approximation

results of [9]. This again leads to minimizing a continuous function of the parameters over a compact space. Either way, the inverse problems we will shortly define will have solutions.

#### 4.1 Statistical Models and Parameter Estimators

In order to carefully define the way in which we will measure the closeness of the data to model values, we must first discuss underlying statistical models for the error present in the data. A proper error model is also key to correctly determining parameter confidence intervals. Much of the discussion here is similar to that in [13], with background on ordinary least squares (OLS) and generalized/weighted least squares (GLS or WLS) given in [22], for example.

We will assume the errors  $\mathcal{E}_j$  are independent, identically distributed with mean zero ( $E[\mathcal{E}_j] = 0$ ) and constant variance  $\text{var}(\mathcal{E}_j) = \sigma_0^2$ ; this process has realizations  $\varepsilon_j$ . Note that we do not assume we know the underlying distributions from which the errors come; we only know the first two central moments as specified. We use this error process in proposing two error models and corresponding parameter estimators.

- **Absolute error:** Here we have the error process  $U_j = u(t_j; 10^{\theta_0}) + \mathcal{E}_j$ , with realizations

$$u_j = u(t_j; 10^{\theta_0}) + \varepsilon_j, \quad (16)$$

where  $\theta_0$  is some hypothesized “true” parameter value (see [22]). We use the ordinary least squares cost function

$$\mathcal{J}_{ols}(\theta) = \sum_{j=0}^{n-1} [u_j - u(t_j; 10^\theta)]^2.$$

The corresponding inverse problem for the logged parameters is then

$$\hat{\theta}_{ols} = \arg \min_{\theta \in Q} \mathcal{J}_{ols}(\theta) = \arg \min_{\theta \in Q} \sum_{j=0}^{n-1} [u_j - u(t_j; 10^\theta)]^2. \quad (17)$$

This function minimizes the distance between the data and model where all observations are considered to have equal importance (weight). Since  $u(t_j; 10^\theta)$  is a continuous function of  $\theta$ ,  $\mathcal{J}_{ols}$  is also a continuous function of  $\theta$ , which means we are minimizing a continuous function of  $\theta$  over a compact set  $Q$ , and thus this inverse problem has a solution.

- **Relative error:** Here we have the error process  $U_j = u(t_j; 10^{\theta_0}) + u(t_j; 10^{\theta_0})\mathcal{E}_j$  with realizations

$$u_j = u(t_j; 10^{\theta_0}) + u(t_j; 10^{\theta_0})\varepsilon_j. \quad (18)$$

For this case, we construct the generalized (weighted) least squares cost function (as per, e.g., [22])

$$\mathcal{J}_{gls}(\theta) = \sum_{j=0}^{n-1} w_j^2 [u_j - u(t_j; 10^\theta)]^2$$

where we define the weights  $w_j = u(t_j; 10^\theta)^{-1}$ . In this case, since we are examining a relative error model (18), these weights take into account the unequal quality of observations; dividing by the function value has a “normalizing” effect on the errors, accounting for the scale differences which may be present in the errors at larger versus smaller model values.

We now wish to find  $\theta$  such that  $\mathcal{J}_{gls}(\theta)$  is minimized. We can either solve this directly, or by using an iterative procedure in order to estimate  $\hat{\theta}_{gls}$  (since the weights must also be estimated). We will use an iterative method, described as follows (see [22] and references therein for convergence details):

1. Define  $\hat{\theta}^0 = \hat{\theta}_{ols}$ , and set  $k = 0$ .
2. Form the weights  $\hat{w}_j = u(t_j; 10^{\hat{\theta}^k})^{-1}$ , using weight thresholding (described below).
3. Re-estimate  $\hat{\theta}_{gls}$  by solving

$$\hat{\theta}^{k+1} = \arg \min_{\theta \in Q} \sum_{j=0}^{n-1} \hat{w}_j^2 [u_j - u(t_j; 10^\theta)]^2$$

to obtain the  $k + 1$  estimate  $\hat{\theta}^{k+1}$  for  $\hat{\theta}_{gls}$ .

4. Set  $k = k + 1$  and return to Step 2. Terminate when successive estimates for  $\hat{\theta}_{gls}$  are sufficiently close, or when one has iterated 20 times. For our problem, our “sufficiently close” criterion was found by determining if  $\|\hat{\theta}^{k+1} - \hat{\theta}^k\|_\infty \leq 10^{-3}$ , where  $\|\theta\|_\infty$  is the maximum component of the given vector  $\theta$ . The parameter values being estimated are all log-scaled, and are thus on the order of  $[10^{-1}, 10^1]$ . This puts the stopping criterion at two orders of magnitude less than the smallest log-scaled parameter value, which is sufficient in our problem.

Even though we have removed all data points with absolute value under  $5 \times 10^{-6}$ , we still account for the (now unlikely) possibility that some model values may still end up small in absolute value. Thus, we incorporate thresholding on the weights to keep from dividing by zero. We take a threshold value of  $1 \times 10^{-10}$ , as this is almost certainly below the threshold of significance in terms of the model displacements. Then, for all indices  $\bar{j} \in \{k \mid |u(t_k; 10^{\hat{\theta}})| < 1 \times 10^{-10}\}$ , we set  $\hat{w}_{\bar{j}} = 1 \times 10^{10}$ . This is done each time the weights are re-estimated in Step 2 of the iterative process.

With weight thresholding, we are assured that the iterative process is possible numerically. Thus, similar to the ordinary least squares case, at each step  $k$  in the iterative GLS estimation process we are minimizing a continuous function of  $\theta$  over a compact parameter space  $Q$ , and thus the inverse problem in each iteration will have a solution. Also, as long as the iterative process is carried out sufficiently many times, under certain conditions the weights will converge  $\hat{w}_j \rightarrow u(t_j; 10^{\hat{\theta}_{gls}})^{-1}$  (see, e.g., [22]).

#### 4.1.1 Optimization considerations

As in [13], we used the Matlab routine `lsqnonlin` for our optimization routine to solve for  $\hat{\theta}_{ols}$  and  $\hat{\theta}_{gls}$ . We used the trust-region-reflective (TRR) algorithm that is built in; as our previous effort in [13] demonstrated, the Levenburg-Marquardt option was slower than TRR and did not give us better results. Since we are using at least one relaxation time, we do not consider `fmincon` which we have shown to be ineffective in estimating relaxation times.

In order to start the optimization routines for computing  $\hat{\theta}_{ols}$ , we must provide initial parameter values (for  $\hat{\theta}_{gls}$  we use the estimated value for  $\hat{\theta}_{ols}$  as our initial guess). From a perusal of the viscoelastic materials literature, our experience with the previous conceptual work, and from some manual examination on the current data sets, we chose the initial values as follows:

$$G = 4.5 \times 10^3 \text{ Pa}, \quad G_1 = 5 \text{ Pa} \cdot \text{s}, \quad \zeta_1 = 2.8 \times 10^4 \text{ Pa}, \quad \tau_1 = 0.06 \text{ s}, \quad A = -1.7 \times 10^{-4} \text{ m}, \quad \Upsilon = -0.01 \text{ s}.$$

As log-scaled values (c.f. (15)), this gives us

$$\theta_{gls}^0 = (3.6532, 0.6990, 4.4472, -1.2218, -3.7696, -2)^T.$$

#### 4.1.2 Residuals

We will also include residual plots to assist in analysis of the model fit to data, and to indicate which error model best describes the error in the data. Residuals give a sense for the model fit to data, but more importantly the residuals can give an indication [22] regarding the appropriateness of our error model. If the absolute residuals seem to be randomly dispersed around the horizontal axis and form a horizontal band around that axis, then the absolute error model may be correct. On the other hand, if the (modified) relative residuals seem to be randomly dispersed, then the relative error model may be correct. We define the following:

- **Absolute residuals** are computed as  $r_j = u_j - u(t_j; 10^{\hat{\theta}})$ , where  $\hat{\theta}$  is the particular parameter estimate being considered.
- **Relative residuals** are computed as  $r_j = \hat{w}_j(u_j - u(t_j; 10^{\hat{\theta}}))$  where  $\hat{w}_j = u(t_j; 10^{\hat{\theta}})^{-1}$  and the  $\hat{w}_j$  are thresholded in the same manner as discussed earlier.

## 4.2 Inverse problem results, $N_p = 1$

We now demonstrate the ability of our model to match data. For this purpose, we will take a single relaxation time ( $N_p = 1$ ) as that is enough to show model fidelity to data. We run both the absolute (OLS) and relative (GLS) error models on a sample data set using a 264 g loading weight. We will report parameter estimates, standard errors and confidence intervals, plots of model fits to data, plots of residuals versus time, and plots of residuals versus model values. We use these elements in order to recommend error models.

Standard errors (and corresponding confidence intervals) are computed using asymptotic error theory. For the absolute error model, the process is the same as that which we used in [13], and is also described in [22, Ch. 3]; for the relative error model, the corresponding asymptotic error methodology is discussed in [22, Ch. 3]. Since the theory is common enough, we do not reiterate it here and refer interested readers to the aforementioned references.

We have also examined parameter estimation using data sampled at different rates. This allowed for a study of whether the parameter estimates and associated confidence intervals remain consistent as the number of data points is reduced. Using fewer data points is also a way of decreasing computational times for the inverse problems. We ran the inverse problem on each data set and using each error model using all the data points (1024 Hz) and using every other data point (512 Hz), as discussed at the beginning of Section 4.

Numerical results show that the results for data sampled at 1024 Hz is consistent with those found for the data sampled at 512 Hz. Hence, we report only the results for data sampled at 512 Hz (all results for data sampling at 1024 Hz are available in [14]). The parameter estimates and confidence intervals (see [10, 11, 13, 16, 22] for information on computing confidence intervals), obtained from the inverse problems using OLS and GLS, are shown in Tables 1-2. We observe from these two tables that the standard errors for the GLS case is larger than in the

Table 1: Shear optimization results and confidence analysis for OLS on a 264 g data set using every other data point.

Param.	Estimate	SE	CI95
$\log_{10}(G)$	3.5431	0.2498	(3.0469, 4.0393)
$\log_{10}(G_1)$	0.3753	0.3227	(-0.2657, 1.0164)
$\log_{10}(\tau_1)$	-1.4450	0.2474	(-1.9364, -0.9535)
$\log_{10}(\zeta_1)$	4.4761	0.0294	(4.4178, 4.5345)
$\log_{10}(-A)$	-3.7501	0.0071	(-3.7643, -3.7360)
$\log_{10}(-\Upsilon)$	-2.1813	0.2779	(-2.7334, -1.6293)

Shear modulus dynamic analog  $G_0 = 33.423$  kPa

Table 2: Shear optimization results and confidence analysis for GLS on a 264 g data set using every other data point.

Param.	Estimate	SE	CI95
$\log_{10}(G)$	3.8649	1.0435	(1.7922, 5.9377)
$\log_{10}(G_1)$	0.5449	0.3561	(-0.1625, 1.2523)
$\log_{10}(\tau_1)$	-1.0217	1.0543	(-3.1161, 1.0726)
$\log_{10}(\zeta_1)$	4.4171	0.2918	(3.8375, 4.9967)
$\log_{10}(-A)$	-3.8026	0.0119	(-3.8263, -3.7789)
$\log_{10}(-\Upsilon)$	-1.6729	1.3806	(-4.4153, 1.0695)

Shear modulus dynamic analog  $G_0 = 33.454$  kPa

OLS case. In addition, we see that the standard error for  $G_1$  is on the same order of magnitude as the parameter estimate itself for both the OLS and GLS results, and the standard errors for  $\tau_1$  and  $\Upsilon$  in the GLS case are also on the same order of magnitude as their corresponding estimates. This is consistent with the sensitivity results, where the model output is less sensitive to  $G_1$ ,  $\tau_1$  and  $\Upsilon$  than to  $G$ ,  $\zeta_1$ , and  $A$  (more details are available in [14]).

Model fits as well as residual plots are shown in Figure 3. In all cases, the model fits to data are good. In the bottom row of Figure 3, the residuals versus model plots are not noticeably different between the OLS and GLS cases. The initial indication is that we have more confidence in the OLS results. However, the residual versus time plots (middle row of Figure 3) raise cause for concern. In the OLS residual versus time plots, there is a noticeable “fan” structure for early times. However, for the GLS error model, the residual versus time plots do not show a fan structure and are fairly randomly distributed. Since this indicates that the OLS error model may not be correct, we are inclined to recommend the GLS error model so that we do not mistakenly overstate our confidence in the parameter estimates, which we could do if we used the parameter estimates from the possibly-wrong OLS case.

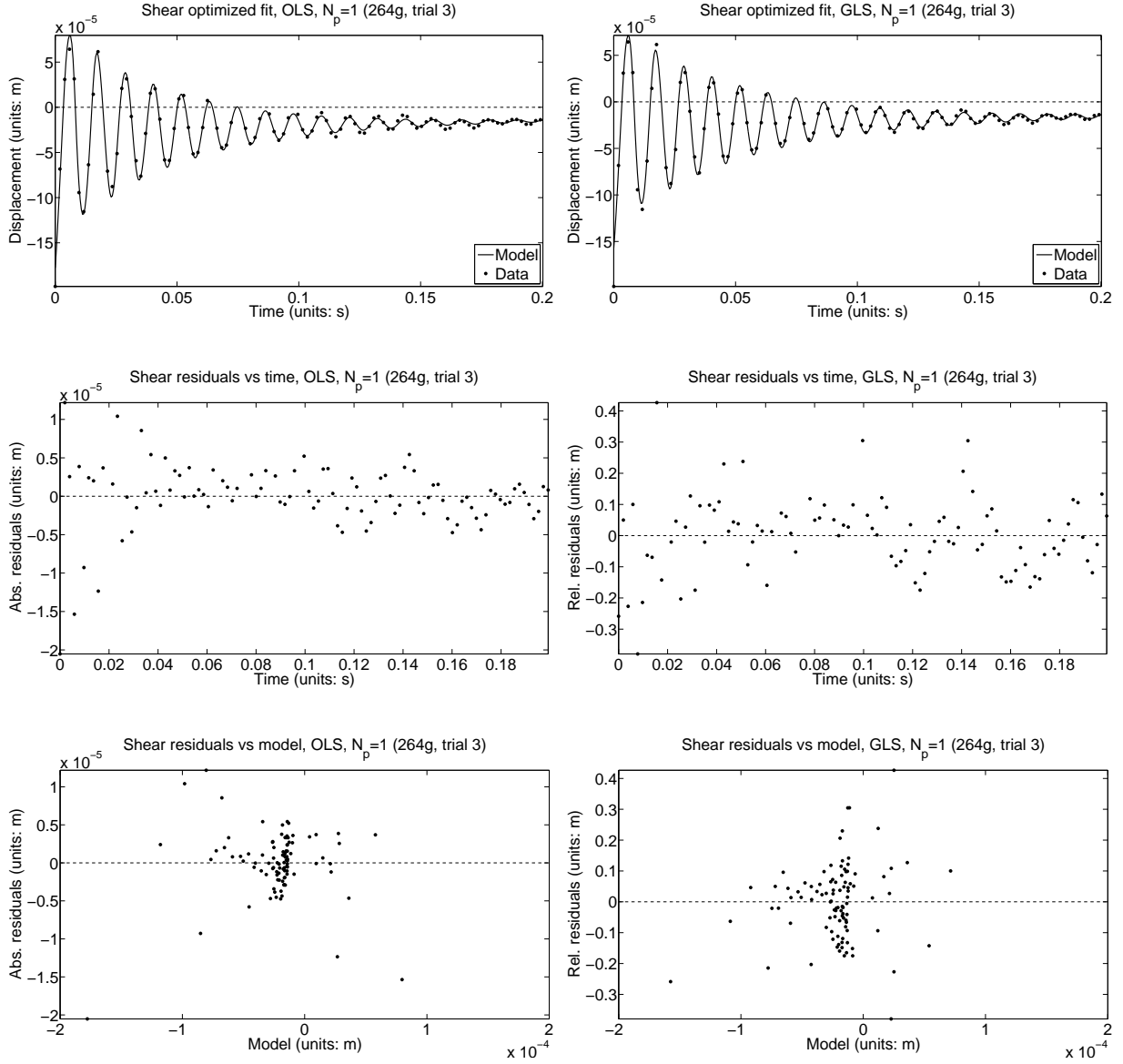


Figure 3: Shear data fit using data sampled at 512 Hz,  $N_p = 1$ , weight 264 g. (left) OLS results. (right) GLS results.



## 5 Discussion and Future Work

We have developed an updated one-dimensional viscoelastic model for tissue and have used experimental data from a simple homogeneous gel phantom to test the ability of our model to describe wave propagation in the medium. The data were generated from a drop experiment designed to produce oscillations in the gel of a magnitude comparable to that produced by blood flow in a stenosed coronary artery impacting the vessel wall, a disturbance which results in shear wave propagating away from the vessel walls downstream of the blockage. In our inverse problem results as discussed in Section 4.2, we have shown an ability to consistently model the wave propagation using different error models and at different data sampling frequencies, obtaining good fits to data in all of our inverse problems. In addition to a good fit, though, we also examined statistical properties of the parameter estimators as well as residual plots to gain more insight into the proper error model for the shear data set. This is necessary, since a correct error model is essential in order to apply the asymptotic error theory properly and thus obtain correct confidence intervals. We recommend taking the more conservative route and using the GLS parameter estimates; even though the GLS estimates had larger standard errors, there were indications from the residual versus time plots for OLS that the OLS model is not correct. Overall, we have successfully demonstrated the ability of mathematical model to accurately describe the data from laboratory experiments using a homogenous tissue-mimicking material gel phantom. A linear viscoelastic constitutive relationship, i.e., (14b), was adequate. This is a significant achievement, as all the work previously discussed was limited to inverse problems on simulated data or data that was not from the impulse-type experiments.

We do note that both the model and experiments that we studied here, though quite useful as a starting point, are limited in replicating reality. Two different paths are the likely next steps. First, we are currently examining a two-dimensional model and corresponding experimental configurations. Experiments are currently in progress to produce a two-dimensional wave from different points in the medium and with different detection points along the outer wall of the phantom. It is conceivable that the one-dimensional parameters could be used as a rough first approximation in a corresponding two-dimensional code, which would allow us to focus on trying to determine the location of the wave generation in the medium. Also, these parameter values could be used in a model of wave propagation in another conceptual device designed to mimic a constricted artery and the waves that result from passing fluid through a constricted pipe in the center of the medium. Therefore in the slightly longer term, we will also likely need to conduct an inverse problem using a two-dimensional model and corresponding data. These one-dimensional results will provide a starting point for parameters in that inverse problem, hopefully decreasing runtime and the time it takes to find viable parameters. The same issues discussed here (sensitivity to parameters, data frequency, number of relaxation times) will again be of concern for the two-dimensional problem. Future efforts will also involve scaling up all these experiments to larger phantoms and then to some sort of actual tissue sample experiments.

Second, the work to this point has still been focused on the simplest problem, that of a homogeneous medium. A clear next step would be adding inhomogeneous features to the gel phantom to mimic different types of tissue in the chest cavity. This would likely be formulated initially in the one-dimensional case, so that we could study the model responses in a simpler framework before moving to a more complicated two-dimensional case. We can increase the number of internal variables to accommodate different material relaxation properties. The model also allows changes to the material parameters; for example, we could use piecewise-defined constants to represent different types of tissue. These two options represent reasonable directions for the next stages of investigation.

## 6 Acknowledgements

This research was supported in part (HTB,SH,ZRK) by Grant Number R01AI071915-09 from the National Institute of Allergy and Infectious Diseases, in part (HTB,SH,ZRK) by the Air Force Office of Scientific Research under grant number AFOSR FA9550-12-1-0188, in part (ZRK) by the Department of Education with a GAANN Fellowship under grant number P200A070386, in part (CK,SS,JW) by the Engineering and Physical Sciences Research Council EP/H011072/1, and in part (MBr,SG(PI),MBi) by the Engineering and Physical Sciences Research Council EP/H011285/1. In addition, the authors are grateful to the two anonymous referees for their helpful comments and constructive suggestions which led to an improved version of the paper.

## References

- [1] M. Ainsworth, P. Monk, and W. Muniz. Dispersive and dissipative properties of discontinuous Galerkin finite element methods for the second-order wave equation, *Journal of Scientific Computing*, **27** (2006), 5–40.

- [2] M. Akay, Noninvasive detection of coronary artery disease using advanced signal processing methods, PhD Dissertation, Rutgers University, Piscataway, NJ, 1990.
- [3] M. Akay, Y. Akay, W. Welkowitz, J. Semmlow, and J. Kostis, Application of adaptive filters to noninvasive acoustical detection of coronary occlusions before and after angioplasty, *IEEE Trans. on Biomed. Eng.*, **39** (1992), 176–184.
- [4] M. Akay, Y. Akay, W. Welkowitz, J. Semmlow, and J. Kostis, Noninvasive detection of coronary artery disease using neural networks, *Proc. IEEE Eng. in Med. & Biol. Soc.*, (1991), 1434–1435.
- [5] M. Akay, M. Bauer, J. Semmlow, W. Welkowitz, and J. Kostis, Analysis of diastolic heart sounds before and after angioplasty, *Proc. IEEE Eng. in Med. & Biol. Soc.*, (1988), 257–260.
- [6] M. Akay, W. Welkowitz, J. Semmlow, and J. Kostis, Application of the ARMA method to acoustic detection of coronary artery diseases, *Med. & Biol. Eng. & Comput.*, **29** (1991), 365–372.
- [7] H.T. Banks, *A Functional Analysis Framework for Modeling, Estimation and Control in Science and Engineering*, CRC Press, Boca Raton London New York, 2012.
- [8] H.T. Banks, J.H. Barnes, A. Eberhardt, H. Tran, and S. Wynne, Modeling and computation of propagating waves from coronary stenoses, *Comp. and Appl. Math.*, **21** (2002), 767–788.
- [9] H.T. Banks and K. Bihari, Modelling and estimating uncertainty in parameter estimation, *Inverse Problems*, **17** (2001), 95–111.
- [10] H.T. Banks and B.G. Fitzpatrick, Inverse problems for distributed systems: statistical tests and ANOVA, LCDS/CCS Rep. 88-16, July, 1988, Brown University; *Proc. International Symp. on Math. Approaches to Envir. and Ecol. Problems*, Springer Lecture Notes in Biomath., **81** (1989), 262–273.
- [11] H.T. Banks, K. Holm and D. Robbins, Standard error computations for uncertainty quantification in inverse problems: Asymptotic theory vs. Bootstrapping, CRSC-TR09-13, N.C. State University, June 2009; Revised May 2010; *Math. and Comp. Modelling*, **52** (2010), 1610–1625.
- [12] H.T. Banks, S. Hu, Z.R. Kenz, A brief review of elasticity and viscoelasticity for solids, *Adv. in Applied Math. and Mech.*, **3** (2011), 1–51.
- [13] H.T. Banks, S. Hu, Z.R. Kenz, C. Kruse, S. Shaw, J.R. Whiteman, M.P. Brewin, S.E. Greenwald and M.J. Birch, Material parameter estimation and hypothesis testing on a 1D viscoelastic stenosis model: Methodology, CRSC-TR12-09, N.C. State University, April 2012; *J. Inverse and Ill-Posed Problems*, **21** (2013), 25–57; DOI 10.1515/jip-2012-0081.
- [14] H.T. Banks, S. Hu, Z.R. Kenz, C. Kruse, S. Shaw, J.R. Whiteman, M.P. Brewin, S.E. Greenwald and M.J. Birch, Model validation for a noninvasive arterial stenosis detection problem, CRSC-TR12-22, N.C. State University, December 2012.
- [15] H.T. Banks, Z.R. Kenz and W.C. Thompson, A review of selected techniques in inverse problem nonparametric probability distribution estimation, *J. of Inverse and Ill-Posed Problems*, **20** (2012), 429–460; DOI 10.1515/jip-2012-0037.
- [16] H.T. Banks, Z.R. Kenz and W.C. Thompson, An extension of RSS-based model comparison tests for weighted least squares, CRSC-TR12-18, N. C. State University, Raleigh, NC, August, 2012; *Intl. J. Pure and Appl. Math.*, **79** (2012), 155–183.
- [17] H.T. Banks and N. Luke, Modeling of propagating shear waves in biotissue employing an internal variable approach to dissipation, *Communication in Computational Physics*, **3** (2008), 603–640.
- [18] H.T. Banks, N. Medhin, and G. Pinter, Multiscale considerations in modeling of nonlinear elastomers, *Inter. J. for Comp. Methods in Eng. Science and Mechanics*, **8** (2007), 53–62.
- [19] H.T. Banks, N. Medhin, and G. Pinter, Nonlinear reptation in molecular based hysteresis models for polymers, *Quarterly of Applied Math.*, **62** (2004), 767–779.
- [20] H.T. Banks and G.A. Pinter, A probabilistic multiscale approach to hysteresis in shear wave propagation in biotissue, *Multiscale Modeling and Simulation*, **3** (2005), 395–412.

- [21] H.T. Banks and J.R. Samuels, Jr, Detection of cardiac occlusions using viscoelastic wave propagation, *Advances in Appl. Math. and Mech.*, **1** (2009), 1–28.
- [22] H.T. Banks and H.T. Tran, *Mathematical and Experimental Modeling of Physical and Biological Processes*, CRC Press, Boca Raton, FL, 2009.
- [23] J.D. De Basabe, M.K. Sen, and M.F. Wheeler, The interior penalty discontinuous Galerkin method for elastic wave propagation: grid dispersion, *Geophys J. Int.*, **175** (2008), 83–93.
- [24] A.O. Borisjuk, Noise field in the human chest due to turbulent flow in a larger blood vessel, *Flow, Turbulence and Combustion*, **61** (1999), 269–284.
- [25] A.O. Borisjuk, Experimental study of noise produced by steady flow through a simulated vascular stenosis, *J. of Sound and Vibration*, **256** (2002), 475–498.
- [26] A.O. Borisjuk, Model study of noise field in the human chest due to turbulent flow in a larger blood vessel, *J. of Fluids and Structures*, **17** (2003), 1095–1110.
- [27] M.P. Brewin, M.J. Birch, S.E. Greenwald, et al., Characterization of the uniaxial elastic properties of an agar-based tissue mimicking material, *in preparation*.
- [28] S. Catheline, J.-L. Gennisson, G. Delon, M. Fink, R. Sinkus, S. Abouelkaram, and J. Culioli, Measurement of viscoelastic properties of homogeneous soft solid using transient elastography: an inverse problem approach, *J. Acoust. Soc. Am.*, **116** (2004), 3734–3741.
- [29] S. Catheline, L. Sandrin, J.-L. Gennisson, M. Tanter, and M. Fink, Ultrasound-based noninvasive shear elasticity probe for soft tissues, *IEEE Ultrasonics Symposium*, **2** (2000), 1799–1801.
- [30] S. Chen, M. Fatemi, and J. Greenleaf, Quantifying elasticity and viscosity from measurement of shear wave speed dispersion, *J. Acoust. Soc. Am.*, **115** (2004), 2781–2785.
- [31] S. Chen, M. Urban, C. Pislaru, R. Kinnick, Y. Zheng, A. Yao, and J. Greenleaf, Shearwave dispersion ultrasound vibrometry (SDUV) for measuring tissue elasticity and viscosity, *IEEE Trans. on Ultrason., Ferroelectrics, and Freq. Contr.*, **56** (2009), 55–62.
- [32] T. Cheng, Diastolic murmur caused by coronary artery stenosis, *Ann. Int. Med.*, **72** (1970), 543.
- [33] T. Defieux, G. Montaldo, M. Tanter, Shear wave spectroscopy for in vivo quantification of human soft tissues visco-elasticity, *IEEE Trans. on Medical Imag.*, **28** (2009), 313–322.
- [34] B. El-Asir, L. Khadra, A. Al-Abbasi, M. Mohammed, Time-frequency analysis of heart sounds, *Proc. IEE TENCON*, (1996), 553–558.
- [35] Y.C. Fung, *Biomechanics: Mechanical Properties of Living Tissues*, Springer-Verlag, New York, 1993.
- [36] A. Góral-Wójcicka, W. Borgiel, Z. Małota, and Z. Nawrat, One the acoustic phenomena produced by turbulence in the flowing blood, *Polish J. Med. Phys. & Eng.*, **8** (2002), 29–35.
- [37] A. Karpouk, S. Alglyamov, Y. Illinskii, E. Zabolotskaya, and S. Emelianov, Assessment of shear modulus of tissue using ultrasound radiation force acting on a spherical acoustic inhomogeneity, *IEEE Trans. on Ultrason., Ferroelectrics, and Freq. Contr.*, **56** (2009), 2380–2387.
- [38] C. Kruse, S. Shaw, J.R. Whiteman, et al., High order space-time finite element schemes for acoustic and viscodynamic wave equations with temporal decoupling, *in preparation*.
- [39] T.S. Lee, W. Liao, and H.T. Low, Numerical simulation of turbulent flow through series stenoses, *Inter. J. for Numer. Methods in Fluids*, **42** (2003), 717–740.
- [40] S. Levinson, M. Shinagawa, and T. Sato, Sonoelastic determination of human skeletal muscle elasticity, *J. Biomechanics*, **28** (1995), 1145–1154.
- [41] S. Lundin, R. Metcalf, C. Hartley, Effects of severity and eccentricity of carotid stenosis on pulsatile blood flow, *Proc. Joint EMBS/BMES*, (2003), 1311–1312

- [42] N. Luke, Modeling shear wave propagation in biotissue: An internal variable approach to dissipation, PhD Dissertation, N.C. State University, Raleigh, 2006.
- [43] S.E. Nissen, Application of intravascular ultrasound to characterize coronary artery disease and assess the progression or regression of atherosclerosis, *Am. J. Cardiol.*, **89** (2002), 24B–31B.
- [44] S.E. Nissen and P. Yock, Intravascular ultrasound: novel pathophysiological insights and current clinical applications, *Circulation*, **103** (2001), 604–616.
- [45] N. Owsley and A. Hull, Beamformed nearfield imaging of a simulated coronary artery containing a stenosis, *IEEE Trans. Med. Imaging*, **17** (1998), 900–909.
- [46] N. Owsley, A.J. Hull, M.H. Ahmed, and J. Kassal, A proof of concept experiment for the detection of occluded coronary arteries using array sensor technology, *Engr. in Medicine and Biol. Society*, IEEE 17th Annual Conf., **1** (1995), 145–146.
- [47] V. Padmanabhan and J. Semmlow, A dedicated system for acoustic detection of coronary artery disease, *Proc. Eng. in Med. & Biol. Soc.*, (1992), 457–458.
- [48] T. Pedley, Mathematical modelling of arterial fluid dynamics, *J. of Eng. Math.*, **47** (2003), 419–444.
- [49] C. Prado, S. Ramos, J. Elias, Jr., and M. Rossi, Turbulent blood flow plays an essential localizing role in the development of atherosclerotic lesions in experimentally induced hypercholesterolaemia in rats, *Int. J. Exp. Path.*, **89** (2008), 72–80.
- [50] J. R. Samuels, Jr. Inverse problems and post analysis techniques for a stenosis-driven acoustic wave propagation model, PhD Dissertation, N.C. State University, Raleigh, 2008.
- [51] L. Sandrin, S. Catheline, M. Tanter, X. Hennequin, and M. Fink, Time-resolved pulsed elastography with ultrafast ultrasonic imaging, *Ultrasonic Imaging*, **21** (1999), 259–272.
- [52] J. Sangster and C. Oakley, Diastolic murmur of coronary artery stenosis, *Brit. Heart J.*, **35** (1973), 840.
- [53] J. Semmlow and K. Rahalkar, Acoustic detection of coronary artery disease, *Annu. Rev. Biomed. Eng.*, **9** (2007), 449–469.
- [54] J. Semmlow, W. Welkowitz, J. Kostis, and J. Mackenzie, Coronary artery disease—correlates between diastolic auditory characteristics and coronary artery stenoses, *IEEE Trans. on Biomed. Eng.*, **30** (1983), 136–139.
- [55] C. Taylor, T. Hughes, and C. Zarins, Finite element modeling of three-dimensional pulsatile flow in the abdominal aorta: relevance to atherosclerosis, *Annals of Biomed. Eng.*, **26** (1998), 975–987.
- [56] J. Verburg and E. van Vollenhoven, Phonocardiography: Physical and technical aspects and clinical uses, in *Noninvasive Physiological Measurements* (ed. P Rolfe), Academic Press, London (1979), 213–259.
- [57] H. Vermarien and E. van Vollenhoven, The recording of heart vibrations: a problem of vibration measurement on soft tissue, *Med. & Biol. Eng. & Comput.*, **22** (1984), 168–178.
- [58] A. Voss, A. Mix, and T. Hübner, Diagnosing aortic valve stenosis by parameter extraction of heart sound signals, *Annals of Biomed. Eng.*, **33** (2005), 1167–1174.
- [59] J.-Z. Wang, B. Tie, W. Welkowitz, J. Semmlow, and J. Kostis, Modeling sound generation in stenosed coronary arteries, *IEEE Trans. on Biomed. Eng.*, **37** (1990), 1087–1094.
- [60] J. Wloka, *Partial Differential Equations*, Cambridge University Press, Cambridge, 1987.
- [61] M. Zia, B. Griffel, V. Fridman, C. Saponieri, and J. Semmlow, Noise detection in heart sound recordings, *Conf. Proc. IEEE Eng. Med. Biol. Soc.*, (2011), 5880–5883.